Received: 17 May 2021 | Revised: 16 August 2021 | Accepted: 17 August 2021

DOI: 10.1002/mrm.28997

TECHNICAL NOTE

Magnetic Resonance in Medicine

Accurate free-water estimation in white matter from fast diffusion MRI acquisitions using the spherical means technique

Antonio Tristán-Vega | **Guillem París** | **Rodrigo de Luis-García** | **Santiago Aja-Fernández**

Laboratorio de Procesado de Imagen (LPI), Universidad de Valladolid, Valladolid, Spain

Correspondence
Antonio Tristán-Vega, Universidad de Valladolid, ETSI de Telecomunicación, Campus Miguel Delibes, Valladolid 47011, Spain.
Email: atriveg@lpi.tel.uva.es

Funding information
Ministerio de Ciencia e Innovación, Grant/Award Number: RTI2018-094569-B-I00

Purpose: To accurately estimate the partial volume fraction of free water in the white matter from diffusion MRI acquisitions not demanding strong sensitizing gradients and/or large collections of different b-values. Data sets considered comprise ∼32-64 gradients near $b = 1000\,\mathrm{s/mm^2}$ plus ∼6 gradients near $b = 500\,\mathrm{s/mm^2}$.

Theory and Methods: The spherical means of each diffusion MRI set with the same *b*-value are computed. These means are related to the inherent diffusion parameters within the voxel (free- and cellular-water fractions; cellular-water diffusivity), which are solved by constrained nonlinear least squares regression.

Results: The proposed method outperforms those based on mixtures of two Gaussians for the kind of data sets considered. W.r.t. the accuracy, the former does not introduce significant biases in the scenarios of interest, while the latter can reach a bias of 5%–7% if fiber crossings are present. W.r.t. the precision, a variance near 10%, compared to 15%, can be attained for usual configurations.

Conclusion: It is possible to compute reliable estimates of the free-water fraction inside the white matter by complementing typical DTI acquisitions with few gradients at a *lowb*-value. It can be done voxel-by-voxel, without imposing spatial regularity constraints.

KEYWORDS
diffusion MRI, free water, spherical means, white matter

1 | INTRODUCTION

The estimation of the partial volume fraction (PVF) of free water (FW) inside brain tissues, and specifically inside the white matter (WM), serves two purposes in diffusion MRI: first, eliminating a confounding factor within diffusion tensor imaging (DTI),[1] which emanates from the limited resolution of diffusion weighted images (DWIs).[2] Second, the FW-PVF itself can be a biological marker for the description of tumorous edema, neuro-inflammation, and others.[3,4]

Several techniques for FW-PVF estimation have been proposed that can be classified depending on the kind of DWI collections they employ: micro-structure oriented methods like NODDI,[5] spherical means,[6] or MiSFIT[7] consider multi-shells, that is, few medium–high b-values (∼2–4, up to $10,000\,\mathrm{s/mm^2}$) with ∼64–128 gradient directions each; spectral methods[8,9] manage large sets (∼15) of low–medium

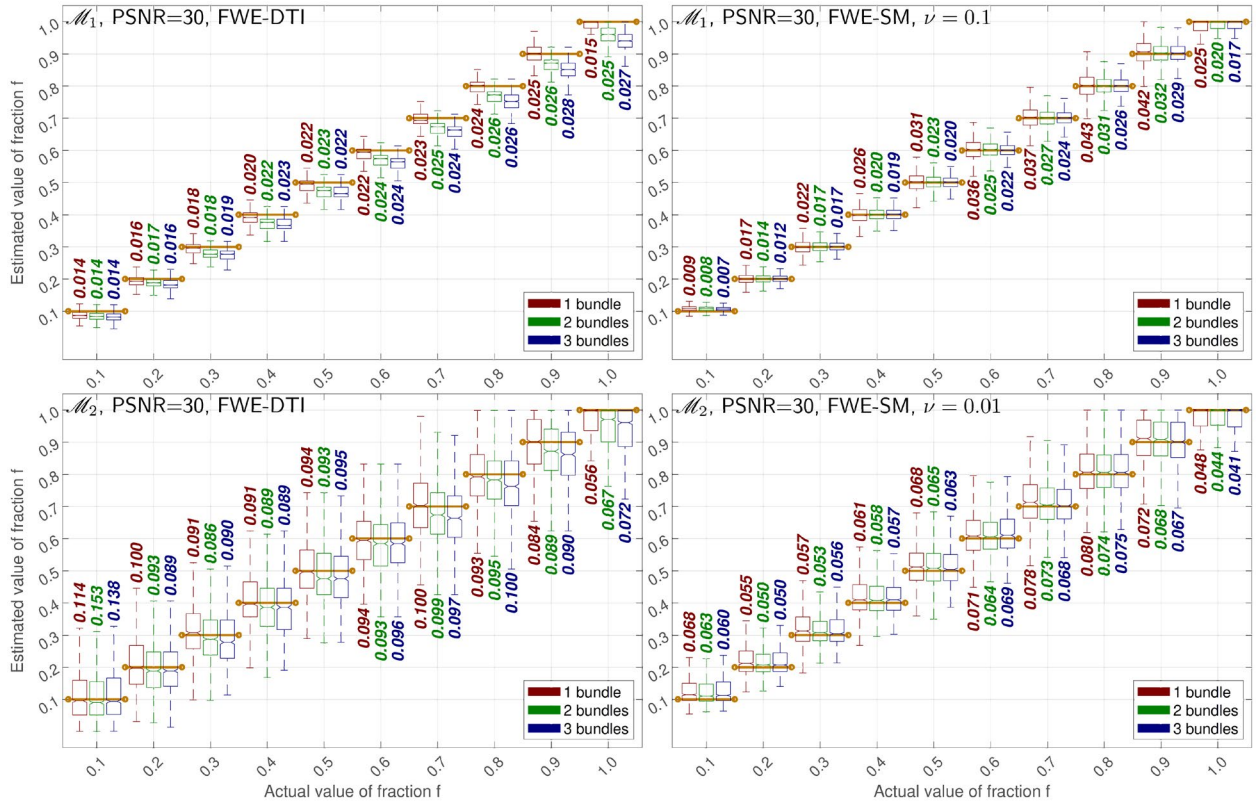

FIGURE 1 Numeric comparison of the accuracy of FWE-DTI (left) versus the proposed FWE-SM (right) based on the model in Equation (7) (for either 1, 2, or 3 simulated fiber bundles). The sampling schemes $\mathscr{M}_1$ (top) and $\mathscr{M}_2$ (bottom) are taken from the Dryad volume, with a typical PSNR=30. Boxes represent the 25% and 75% quantiles of the estimated f; whiskers represent the extreme values; notches represent the median value; the quantity next to each boxplot represents the standard deviation of the corresponding data. All the boxplots are computed over 1000 random samples

b-values (up to $2,500\,\mathrm{s/mm^2}$) with few gradients each (<15); finally, DTI-based methods use either single-shell acquisitions near $1000\,\mathrm{s/mm^2}$[2,3] or they complement this *standard* DTI acquisition with few gradients at a smaller b-value ($\sim 500\,\mathrm{s/mm^2}$).[10]

We are interested here in little demanding acquisitions. Even when single-shell estimates can be reliable if a proper regularization is embedded,[3] it has been shown that these results must be interpreted with care.[11] Since both regularized[10] and unregularized[12] schemes benefit from using a complementary b-value, we will focus on samplings like those in Ref. [10], with ∼32-64 gradient directions at $b \sim 1000\,\mathrm{s/mm^2}$ plus ∼6 gradients at $b \sim 500\,\mathrm{s/mm^2}$. With a 3T, multi-coil device, acquisition times can thus be reduced from 40 to 15 minutes compared to the protocol suggested in Ref. [12].

We propose a method to estimate the FW-PVF voxel wise, without any spatial regularization. It models the DWI as the convolution of a non-parametric fiber orientation distribution function (fODF) with an impulse response that depends on the cellular-water (CW) PVF. This has the additional advantage of releasing our approach of the Gaussian assumption for CW diffusion, which inside the WM is strictly valid only if a unique dominant direction exists.[3] CW-PVF estimation then reduces to a least squares (LS) fitting of two parameters, so that it can be attained from the spherical means of two acquired shells.

2 | THEORY

According to the two-component model in Ref. [2], the signal $S(\mathbf{g}_i, b_i)$ obtained when a diffusion gradient $\mathbf{g}_i$ with b-value b_i is applied becomes the mixture of a CW-PVF, f, plus a FW-PVF, $1-f$:

$$\frac{S(\mathbf{g}_i, b_i)}{S_0} = f \cdot \overbrace{\exp\left(-b_i\, \mathbf{g}_i^T \mathbf{D} \mathbf{g}_i\right)}^{\text{CW}} + (1-f) \cdot \overbrace{\exp\left(-b_i\, D_0\right)}^{\text{FW}}, \quad (1)$$

where S_0 is the unweighted T2 baseline, $\mathbf{D}$ is the 3×3 symmetric diffusion tensor (DT), and D_0 is the diffusivity of FW at body temperature (nearly $3.0 \cdot 10^{-3}\,\mathrm{mm^2/s}$). Provided a collection $\{\mathbf{g}_i, b_i\}_{i=1}^{N}$, $N \gg 7$ is available, Equation (1) can be

solved for seven unknowns: the six free components of $\mathbf{D}$ and f itself. In Ref. [3], a unique b is used for all $\mathbf{g}_i$, which turns the problem ill posed. On the contrary, it is shown in Ref. [12] that a robust estimation of f is feasible voxel-by-voxel by acquiring two shells, that is, two collections of evenly spaced gradients with two different b-values: $\{\mathbf{g}_{i_1}, b_1\}_{i_1=1}^{N/2} \bigcup \{\mathbf{g}_{i_2}, b_2\}_{i_2=1}^{N/2}$.

Equation (1) models either the GM or single-bundled WM.[3] To get rid of the latter limitation, we make use of the representation proposed in Ref. [7], which entails a continuous mixture of tensors in the space of orientations, $\Omega \equiv \{\mathbf{v} \in \mathbb{R}^3 : \|\mathbf{v}\| = 1\}$:

$$\frac{S(\mathbf{g},b)}{S_0} = f \cdot \overbrace{\int\int_{\Omega} \Phi(\mathbf{v}) \exp\left(-b\left(\left(\mathbf{v}^T\mathbf{g}\right)^2\left(\lambda_{\parallel}-\lambda_{\perp}\right)+\lambda_{\perp}\right)\right) d\mathbf{v}}^{\text{CW}} + (1-f)\cdot \overbrace{\exp\left(-bD_0\right)}^{\text{FW}}, \tag{2}$$

where $\Phi(\mathbf{v}) \geq 0$, which sums up to 1 in Ω, is an fODF that accounts for the PVFs of the continuous mixture of WM bundles.

The two parameters $0 \leq \lambda_{\perp} \leq \lambda_{\parallel} \leq D_0$ describe the (distinct) eigenvalues of a prolate DT whose main eigenvector is aligned with $\mathbf{v}$, which can be seen as the impulse response of each WM bundle.[7,13] The key point in Ref. [7] is that, for shells-like samplings, Equation (2) can be averaged over Ω to obtain one spherical mean per measured shell that no longer depends on the fODF:

$$\begin{aligned}\widehat{s}_j &\triangleq \frac{1}{4\pi}\int\int_{\Omega}\frac{S(\mathbf{g},b_j)}{S_0}\,d\mathbf{g}\\ &= f\cdot\frac{\sqrt{\pi}}{2}\exp\left(-b_j\lambda_{\perp}\right)\frac{\operatorname{erf}\left(\sqrt{b_j\left(\lambda_{\parallel}-\lambda_{\perp}\right)}\right)}{\sqrt{b_j\left(\lambda_{\parallel}-\lambda_{\perp}\right)}}\\ &\quad + (1-f)\cdot\exp\left(-b_jD_0\right),\end{aligned} \tag{3}$$

which depends on three unknowns, f, $\lambda_{\parallel}$, and $\lambda_{\perp}$, that need to be solved from $M \geq 3$ equations corresponding to each acquired shell with b-value $\{b_j\}_{j=1}^{M}$. Provided we aim at estimating f from dual b-valued data sets, we first modify the method in Ref. [7] by fixing $\lambda_{\parallel}$ and solving Equation (3) for f and $\lambda_{\perp}$ from the spherical averages $\{\widehat{s}_j\}_{j=1}^{M}$ of $M \geq 2$ shells. The rationale behind this is the low sensitivity observed for $\lambda_{\parallel}$ within the WM in Refs. [7, Figure 2] and [13, Figure 5].

3 | METHODS

3.1 | Numerical resolution of Equation (3)

Let $\mathscr{M} = \bigcup_{j=1}^{M}\{\mathbf{g}_{i_j}, b_j\}_{i_j=1}^{N_j}$ be a multi-shell sampling with M shells and N_j gradient directions each. The j-th spherical mean, $\widehat{s}_j$, is obtained by fitting the samples $\{S(\mathbf{g}_{i_j}, b_j)/S_0\}_{i_j=1}^{N_j}$ in the basis of spherical harmonics (SH), following the numerical approach described in Ref. [14]: if C_0^0 is the DC component of the SH expansion, then $\widehat{s}_j = C_0^0/\sqrt{4\pi}$. Like in Ref. [7], we develop on Equation (3) to isolate f in one term and take logarithms.

The problem reduces to a LS minimization over $M \geq 2$ shells:

$$min_{f,\lambda_{\perp}}\ \frac{1}{2}\sum_{j=1}^{M}\left(\log\left(\frac{\widehat{s}_j-(1-f)e^{-b_jD_0}}{f}\right)+b_j\lambda_{\perp}+\log\left(\frac{2\sqrt{b_j(\lambda_{\parallel}-\lambda_{\perp})}}{\sqrt{\pi}\operatorname{erf}\left(\sqrt{b_j(\lambda_{\parallel}-\lambda_{\perp})}\right)}\right)\right)^2+\nu\frac{\lambda_{\perp}}{\lambda_{\parallel}-\lambda_{\perp}}, \tag{4}$$

where we fix $\lambda_{\parallel} = 2.1\cdot 10^{-3}\,\mathrm{mm^2/s}$ throughout, after the results in Ref. [7, Figure 2]. The penalty term weighted by the constant $\nu \geq 0$ is a second necessary modification to Ref. [7], and promotes prolate convolution kernels when $\mathscr{M}$ is restricted to small b-values. Finally, for the problem to be physically consistent, we need to impose additional constraints to the objective function in Equation (4):

$$f_0 \leq f \leq 1,\ \text{for } f_0 = max_{j=1\ldots M}max\left\{1-\frac{\widehat{s}_j}{e^{-b_jD_0}}, 1-\frac{1-\widehat{s}_j}{1-e^{-b_jD_0}}\right\}; \tag{5}$$

$$0 \leq \lambda_{\perp} \leq \lambda_{\parallel}. \tag{6}$$

Equation (5) ensures the CW-PVF remains in the allowed range [0, 1], meanwhile Equation (6) ensures the convolution kernel is actually prolate. The LS problem described by the objective function (4) and the constraints (5) and (6) is solved by means of a gradient-projection algorithm derived from Ref. [7, Appendix A].

3.2 | Generation of synthetic data

The validation of our proposal is partially based on numeric comparisons over synthetically generated voxels. For each

sample $\{\mathbf{g}_{i_j}, b_j\} \in \mathscr{M}$, the synthetic signal will fit this compound multi-tensor model:

$$S(\mathbf{g}_{i_j}, b_j) = f \cdot S_0 \sum_{k=1}^{3} \alpha_k \exp\left(-b_j \mathbf{g}_{i_j}^T \mathbf{D}_k \mathbf{g}_{i_j}\right) + (1-f) \cdot S_0 \exp\left(-b_j D_0\right), \quad \sum_{k=1}^{3} \alpha_k = 1, \tag{7}$$

which allows simulating WM configurations with either a unique dominant fiber bundle, $\{\alpha_1 \neq 0, 0, 0\}$, two bundles, $\{\alpha_1 \neq 0, \alpha_2 \neq 0, 0\}$, or three bundles $\{\alpha_1 \neq 0, \alpha_2 \neq 0, \alpha_3 \neq 0\}$. In all cases, the non-null α_k are generated as uniform random numbers in [0.4, 0.6], and then normalized to sum to 1. The eigenvalues of each DT, $\mathbf{D}_k$, are designed as Gaussian random variables with mean and standard deviation retrospectively chosen based on the experiment in Figure 3: $\lambda_1 \sim N(1.3, 0.3)$; $\lambda_2 \sim N(0.4, 0.1)$; $\lambda_3 \sim N(0.25, 0.08)$ $(\times 10^{-3}\ \mathrm{mm}^2/\mathrm{s})$. The eigenvectors of $\mathbf{D}_1$ are, respectively, aligned with axes "*x*," "*y*," and "*z*;" those of $\mathbf{D}_2$ are aligned with axes "*y*," "*z*," and "*x*;" those of $\mathbf{D}_3$, with "*z*," "*x*," and "*y*." The whole ensemble is randomly rotated, and both the diffusion signal and the unweighted T2 baseline are contaminated with Rician noise with known PSNR (defined as S_0/σ, with σ^2 the noise power in the complex domain).

3.3 | Materials

Two different data sets have been used for testing:

- From the Dryad data repository (Available: https://datadryad.org/stash/dataset/doi:10.5061/dryad.9bc43), the human data set described in Ref. [15]. It was acquired with a Siemens Trio 3T with resolution $2.5\,\mathrm{mm}^3$ and matrix size $96 \times 96 \times 19$ covering the central part of the brain. Imaging parameters are $\mathrm{TR} = 7,200\,\mathrm{ms}$, $\mathrm{TE} = 116\,\mathrm{ms}$, with a typical PSNR of 30 inside the WM. Among the available b-values, we use a multi-shell scheme $\mathscr{M}_1$ with $M = 8$ shells and $N_j = 33, \forall j$ gradient directions each. The b-values $\{b_j\}_{j=1}^{8}$ are evenly spaced from $b_1 = 200$ to $b_8 = 1600$ in steps of 200 (in $\mathrm{s/mm}^2$). A sub-sampled multi-shell scheme $\mathscr{M}_2$ is obtained from $\mathscr{M}_1$ with just $M = 2$ shells: the first one, with all $\{\mathbf{g}_{i_5}\}_{i_5=1}^{33}$ at $b_5 = 1000\,\mathrm{s/mm}^2$ directly taken from $\mathscr{M}_1$; the second one, by decimating the set $\{\mathbf{g}_{i_2}\}_{i_2=1}^{33}$ at $b_2 = 400\,\mathrm{s/mm}^2$ from $\mathscr{M}_1$ to six gradient directions minimizing the electrostatic repulsion energy (by greedy search). Hence, in $\mathscr{M}_2$, $M = 2$, $N_1 = 33$, $b_1 = 1000\,\mathrm{s/mm}^2$, $N_2 = 6$, $b_2 = 400\,\mathrm{s/mm}^2$.
- A volume acquired with a 3T Philips Achieva at the Universidad de Valladolid (UVa), with a multi-shell scheme $\mathscr{M}_3$ defined by $M = 3$ shells with $N_j = 64, \forall j$ gradient directions each. The respective b-values (in $\mathrm{s/mm}^2$) are $b_1 = 500$, $b_2 = 1000$, and $b_3 = 1500$. The spatial resolution is $1.875^2 \times 2.5\,\mathrm{mm}^3$, with matrix size $128 \times 128 \times 52$ for full-brain coverage. The TE and TR are, respectively, 83 ms and 9000 ms, granting a typical PSNR nearly 20 inside the WM. We obtain an additional multi-shell scheme $\mathscr{M}_4$ with $M = 2$, $N_1 = 64, b_1 = 1000\,\mathrm{s/mm}^2$, $N_2 = 6, b_2 = 500\,\mathrm{s/mm}^2$ by keeping the original shell at $b = 1000\,\mathrm{s/mm}^2$ from $\mathscr{M}_3$ and decimating the shell at $b = 500\,\mathrm{s/mm}^2$.

The WM was roughly segmented by thresholding the fractional anisotropy (FA) at a value of 0.35. The FA was computed in all cases from a DTI fitted to the DWI with regular LS.[16] Besides, the WM was classified in three groups based on Westin's coefficients[16]: linear (C_l), planar (C_p), and spherical (C_s). After initializing three clusters with centroids $[C_l, C_p, C_s] = \{[1,0,0], [0,1,0], [0,0,1]\}$, the C-means algorithm was run until convergence. We can reasonably hypothesize the first cluster corresponds to WM configurations with a unique dominant direction ($\alpha_2 = \alpha_3 = 0$ in Equation (7)), the second one to configurations with two dominant bundles ($\alpha_3 = 0$ in Equation (7)), and the third one to more complex configurations ($\alpha_k \neq 0, \ \forall k$).

4 | RESULTS

The proposed method (hereafter FWE-SM, standing for free-water elimination–spherical means) will be compared to Ref. [12] (hereafter FWE-DTI), as long as it is also aimed at voxel-by-voxel estimation, without spatial regularization, with b-values typical of DTI. According to Section 3.2, we can simulate synthetic voxels for the multi-shell schemes $\mathscr{M}_{1,2,3,4}$ with ground truth values of *f*, so that we can evaluate the performance of each method at scenarios reasonably similar to those expected within the WM of the subjects described in Section 3.3. The respective results are shown in Figures 1 and 2 (the parameter ν in Equation (4) has been empirically fixed in all cases): with the *whole* samplings $\mathscr{M}_1$ and $\mathscr{M}_3$, both methods are precise, with small variances in all cases. In terms of precision, FWE-DTI provides smaller variances for one-bundle configurations, but similar or greater variances for two or three bundles. In terms of accuracy, while FWE-SM remains unbiased for almost all configurations (except for very small *f*), FWE-DTI presents noticeable negative biases for two bundles and three bundles, reaching values near 5%-7% for CW-PVF in the range [0.7, 0.8]. Yet, the main purpose of the present paper is the accurate estimation of *f* from acquisitions more alike $\mathscr{M}_2$ and $\mathscr{M}_4$. In these cases, FWE-SM remains accurate (no noticeable biases appear), with a more subtle effect on the precision than FWE-DTI suffers: note, both in Figures 1 and 2, the heavy increase of boxes and whiskers sizes (ie, 25%/75% quantiles and extreme values), as well as variances, from the

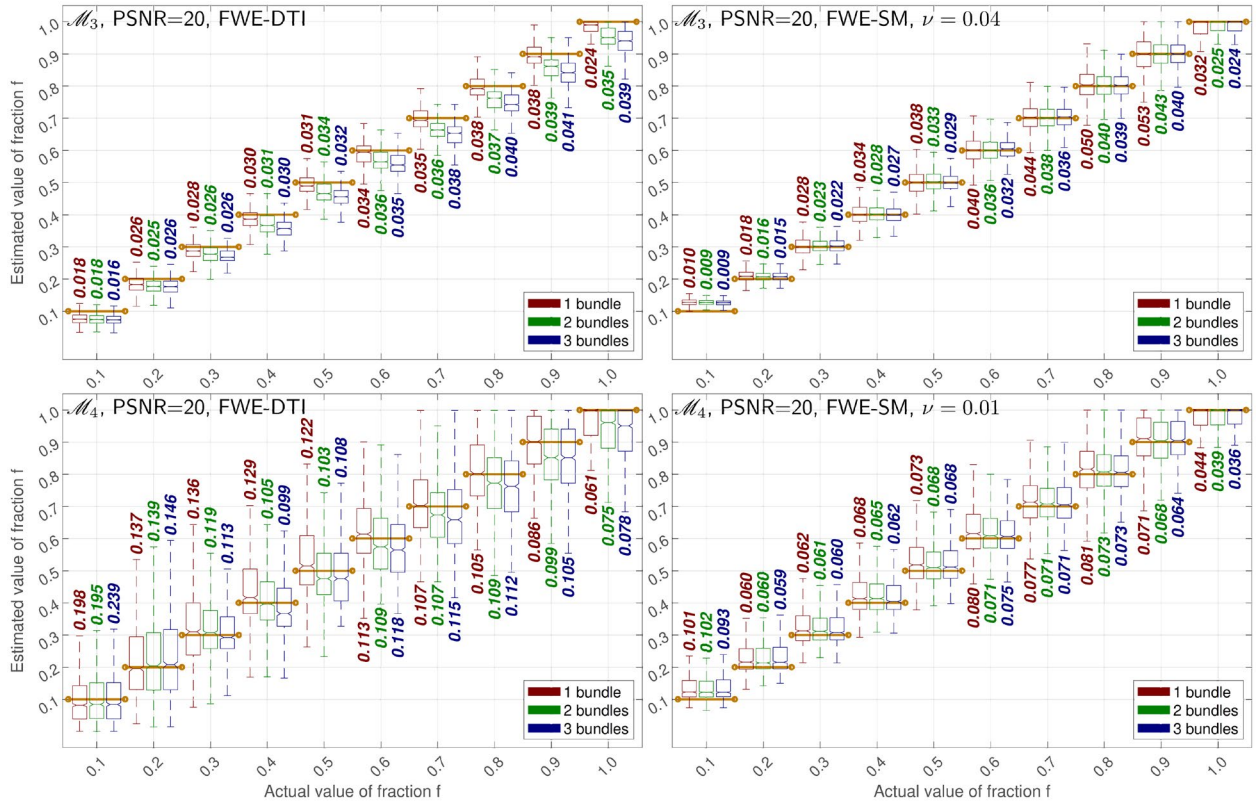

FIGURE 2 Numeric comparison of the accuracy of FWE-DTI (left) versus the proposed FWE-SM (right) based on the model in Equation (7) (for either 1, 2, or 3 simulated fiber bundles). The sampling schemes $\mathcal{M}_3$ (top) and $\mathcal{M}_4$ (bottom) are taken from the UVa volume, with a typical PSNR = 20. The notation is as in Figure 1. All the boxplots are computed over 1000 random samples

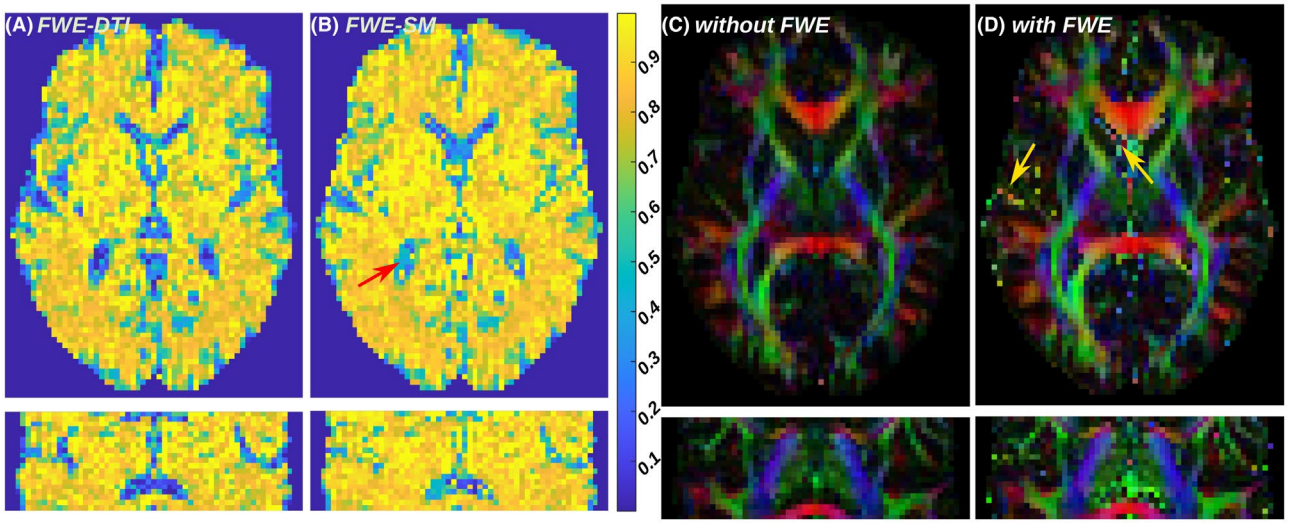

FIGURE 3 CW-PVF in the Dryad volume, f, as estimated with either FWE-DTI (A) or the proposed FWE-SM with $\nu = 0.1$ (B). For the latter, standard color-coded maps based on the first eigenvector of the DTI are shown before (C) and after (D) FW elimination. The central axial and coronal slices are shown in all cases. The red arrow points to CSF voxels for which FWE-SM overestimates f. The yellow arrows point to DTI outliers after FWE in these same regions

top line to the bottom for FWE-DTI, which is not equally dramatic for FWE-SM.

The consistency of FWE-SM for a real data set is checked in Figure 3, where f is calculated for the Dryad volume with the *full* sampling $\mathcal{M}_1$. As it could be predicted from Figure 1, the results from both FWE-DTI and FWE-SM look quite similar throughout the WM. This statement holds also for the GM, the main difference between the two approaches being at

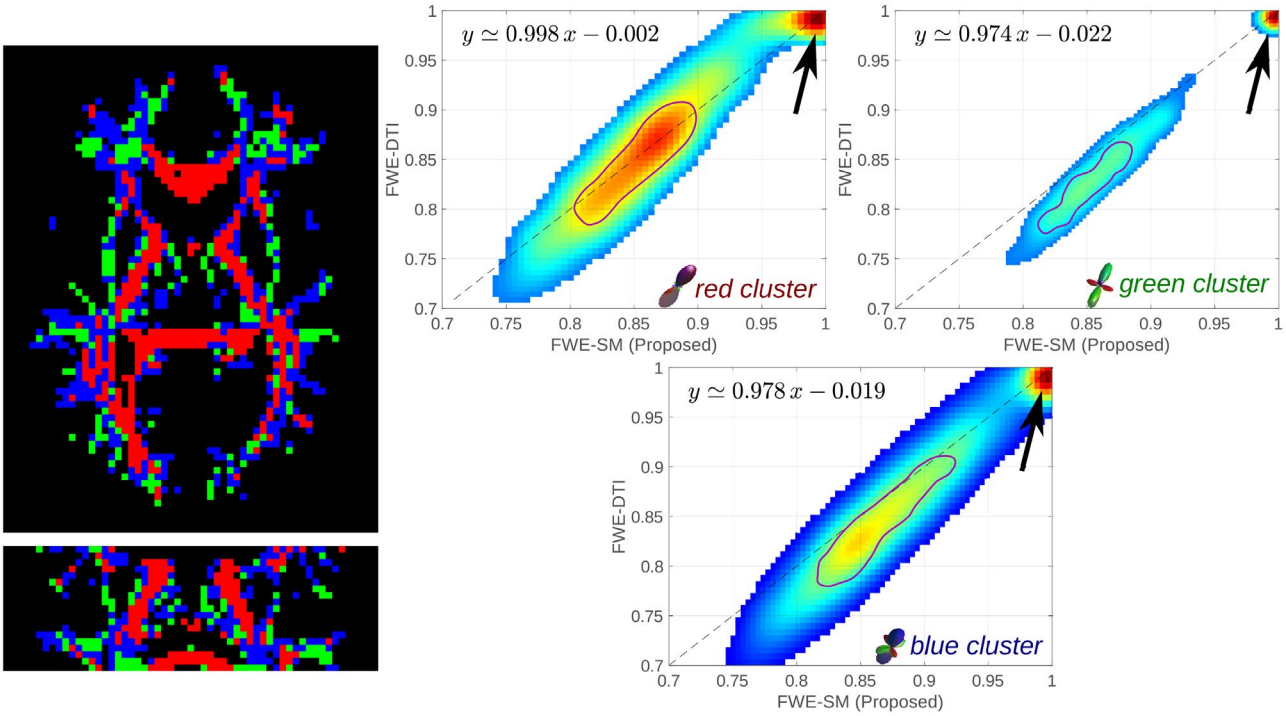

FIGURE 4 WM clustering of the Dryad volume. The 2D histograms compare the CW-PVF, f, computed with either FWE-DTI or the proposed FWE-SM ($\nu = 0.1$) with the *full* sampling $\mathscr{M}_1$, inside each WM cluster. The black arrows point to histogram values coming from the saturation of f to its maximum value of 1. The equations $y = a\,x + b$ are obtained from linear regression, so that b stands for the relative bias of FWE-DTI w. r. t. FWE-SM

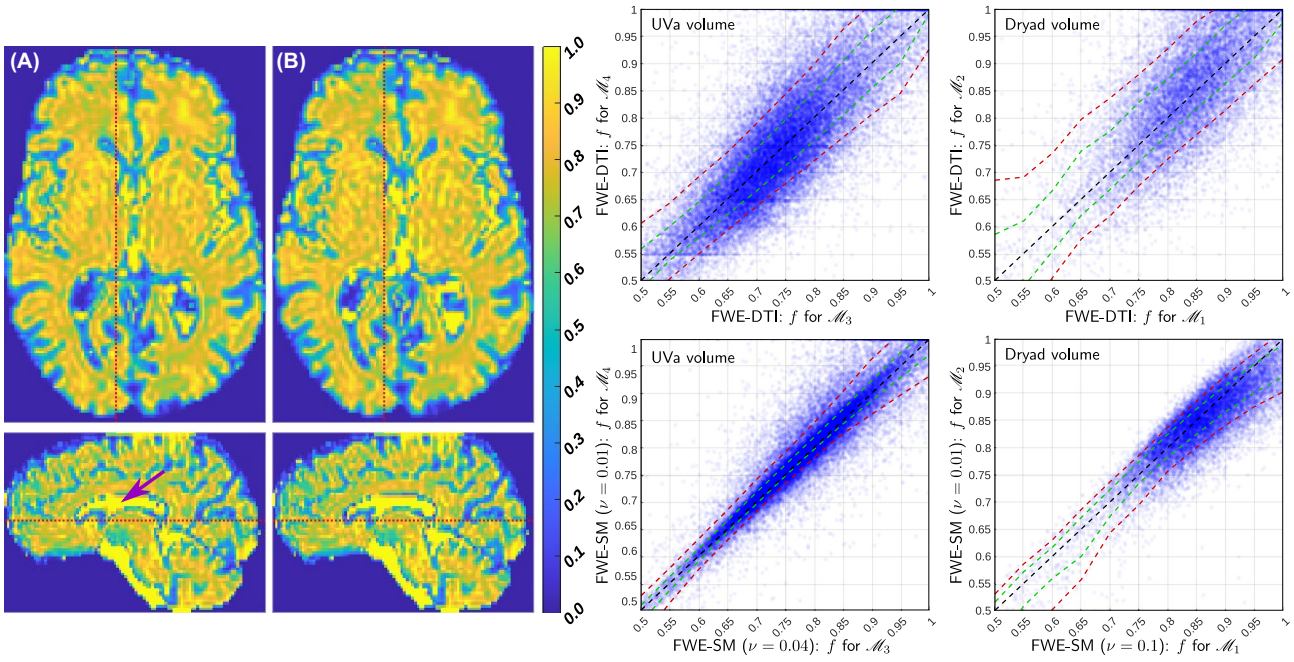

FIGURE 5 Comparison of the estimates of the CW-PVF, f, obtained with either *ad hoc* samplings ($\mathscr{M}_1$, $\mathscr{M}_3$) or DTI-like samplings ($\mathscr{M}_2$, $\mathscr{M}_4$): axial and sagittal slices are shown for the UVa volume, estimated with FWE-SM from (A) $\mathscr{M}_3$ ($\nu = 0.04$), (B) $\mathscr{M}_4$ ($\nu = 0.01$). The scatter plots depict the comparison of the *full* sampled data sets with the sub-sampled data sets, for both test volumes, and for either FWE-DTI or FWE-SM, inside the WM. Green dashed lines represent the 25%/75% quantiles, and red dashed lines represent the 10%/90% quantiles. The purple arrow points to pure CSF voxels, for which the FWE-SM model becomes ambiguous

the CSF (red arrow): in these pure FW regions, our FWE-SM tends to overestimate f, which is also visible in Figure 2 (top, right) for the sampling scheme $\mathcal{M}_3$ (but not really evident in Figure 1 for $\mathcal{M}_1$). Moreover, we can refer to Equation (1), then use standard LS,[16] to compare the DTI estimation either with or without FW elimination as shown in Figure 3C,D. As expected, eliminating the FW compartment does not alter the structure or directionality of the WM bundles, but it notably increases their observed anisotropy (which translates in *brighter colors*). On the other hand, FW elimination is likely to introduce outliers at the CSF (yellow arrows).

To further investigate the behavior observed in Figures 1 and 2, Figure 4 compares FWE-DTI and FWE-SM inside three WM clusters obtained as described in Section 3.3, roughly corresponding to prolate, oblate, or spherical configurations. In all cases, a prominent histogram mode at [1.0, 1.0] is present, likely corresponding to the saturation of f to its maximum value. Obviating this artifact, the histograms demonstrate a strong correlation between both methods with slope approximately 1. While the principal mode for the red cluster (purple contour) is completely over the identity line, the principal modes of the other clusters demonstrate a negative bias of FWE-DTI one order of magnitude above that found inside the red cluster, which is consistent with Figures 1 and 2. The computation of the eigenvalues of the DTI inside the red cluster yields respective values (mean±standard deviation, $\times 10^{-3}\text{mm}^2/\text{s}$): 1.3 ± 0.3; 0.4 ± 0.1; 0.25 ± 0.08.

The final experiment, summarized in Figure 5, is aimed at checking to what extent the performance in the estimation of f worsens when a nearly standard DTI acquisition, like $\mathcal{M}_2$ or $\mathcal{M}_4$, is used instead of an *ad hoc* one, like $\mathcal{M}_1$ or $\mathcal{M}_3$. The estimates obtained for either the Dryad volume with $\mathcal{M}_1$ or the UVa with $\mathcal{M}_3$ are used as a silver standard, and the respective estimates for $\mathcal{M}_2$ and $\mathcal{M}_4$ are compared against it: for the UVa volume, the appearance of the f maps are almost identical with both $\mathcal{M}_3$ and $\mathcal{M}_4$ (the results for the Dryad volume, not shown, are analogous), which translates in a tight fit of the 25% / 75% quantiles of the sub-sampled estimates compared to the silver standard. Although these quantiles spread more for the Dryad volume, probably due to the smaller number of gradients in the shell at $b = 1000\,\text{s/mm}^2$, they still show a much better performance compared to the FWE-DTI approach, whose 10% / 90% quantiles show a great dispersion for the extreme values. Noticeably, the miss estimation at CSF voxels becomes accentuated for the UVa volume, see the purple arrow in Figure 5A.

5 | DISCUSSION AND CONCLUSIONS

The proposed FWE-SM is able to compute accurate estimates of the CW-PVF f from acquisitions comparable to those in DTI studies, at the only expense of acquiring as few as six additional gradients at a lower b-value. This allows to complement, or even improve, such DTI studies with little additional effort. With acquisitions specifically designed for FW elimination, it is as precise as DTI-based methods,[3,10,12] but it remains unbiased in almost all situations. Although the bias for FWE-DTI is predictable in terms of f itself, it directly depends on the number of crossing fibers, which is unknown beforehand. FWE-SM gets rid of this confounding factor by averaging all fiber bundles.

For the fast acquisitions object of study in this paper, the errors committed by FWE-SM may increase to 10% for typical CW-PVF values (in the range of [0.7, 1.0]), or up to 70% for CSF voxels. Although these errors are still below those achievable with FWE-DTI, it is arguable if this accuracy might suffice to describe FW voxel wise. As opposed to Refs. [3, 10], we do not rely on any spatial regularization to provide consistent results, but such techniques could be used by either applying a corresponding penalty to Equation (4) or pre-processing the DWI with some sort of denoising technique. Since using reduced samplings increases the variance of the results without notably biasing them, both approaches should help improving the voxel-wise accuracy.

On the other hand, our proposal reduces the number of degrees of freedom by fixing $\lambda_{\parallel}$ in Equation (2), which compels using a regularization parameter ν we need to fix. Fortunately, we have empirically checked that this parameter is much less sensitive to the PSNR than it is to the sampling scheme, so that it can be fixed, based on synthetic experiments like those in Figures 1 and 2, for the entire volume (like we did throughout the paper). Moreover, since we are focusing on acquisitions like $\mathcal{M}_2$ and $\mathcal{M}_4$, we can recommend a standard value $\nu = 0.01$.

Finally, the proposed method fails at estimating f inside voxels with large CSF contamination, for which the convolution model in Equation (2) becomes ambiguous.[7] This illness compromises its validity for the study of pathological conditions like edema or WM hyperintensities, although *ad hoc* corrections like those in Ref. [12] could be thought of in the presence of abnormally large $\lambda_{\perp}$ and small f.

ACKNOWLEDGEMENTS

This work was supported by Ministerio de Ciencia e Innovación (Spain) through research grant RTI2018-094569-B-I00.

CONFLICT OF INTEREST

The authors declare there is no conflict of interest.

DATA AVAILABILITY STATEMENT

All methods tested in this paper, including a clone of the FWE-DTI,[12] have been coded using Matlab©as a part of the dMRI-Lab toolbox (the FWE-DTI is implemented as atti2

freewaterTensor.m, and the FWE-SM as atti2micro.m; the greedy search algorithm for gradients decimation is coded as decimateGradients.m). It can be freely downloaded from: http://www.lpi.tel.uva.es/dmrilab.

ORCID

Antonio Tristán-Vega http://orcid.org/0000-0002-4614-2501
Guillem París https://orcid.org/0000-0002-1564-1199
Rodrigo de Luis-García https://orcid.org/0000-0001-5023-6490
Santiago Aja-Fernández https://orcid.org/0000-0002-5337-5071

REFERENCES

1. Bergamino M, Pasternak O, Farmer M, Shenton M, Hamilton JP. Applying a free-water correction to diffusion imaging data uncovers stress-related neural pathology in depression. *NeuroImage Clin*. 2015;10:336-342.
2. Pierpaoli C, Jones DK. Removing CSF Contamination in Brain DT-MRIs by Using a Two-Compartment Tensor Model. In *11th Conference of the International Society of Magnetic Resonance in Medicine (ISMRM)*. Melbourne, Australia, 2004:1215.
3. Pasternak O, Sochen N, Gur Y, Intrator N, Assaf Y. Free water elimination and mapping from diffusion MRI. *Magn Reson Med*. 2009;62:717-730.
4. Pasternak O, Westin CF, Bouix S, et al. Excessive extracellular volume reveals a neurodegenerative pattern in schizophrenia onset. *J NeuroSci*. 2012;32:17365-17372.
5. Zhang H, Schneider T, Wheeler-Kingshott CA, Alexander DC. NODDI: practical in vivo neurite orientation dispersion and density imaging of the human brain. *NeuroImage*. 2012;61:1000-1016.
6. Kaden E, Kelm ND, Carson RP, Does MD, Alexander DC. Multi-compartment microscopic diffusion imaging. *NeuroImage*. 2016;139:346-359.
7. Tristán-Vega A, Aja-Fernández S. Efficient and accurate EAP imaging from multi-shell dMRI with micro-structure adaptive convolution kernels and dual Fourier integral transforms (MiSFIT). *NeuroImage*. 2021;227:117616
8. De Luca A, Leemans A, Bertoldo A, Arrigoni F, Froeling M. A robust deconvolution method to disentangle multiple water pools in diffusion MRI. *NMR Biomed*. 2018;31:e3965
9. Wong SM, Backes WH, Drenthen GS, et al. Spectral diffusion analysis of intravoxel incoherent motion MRI in cerebral small vessel disease. *J Magn Reson Imaging*. 2020;51:1170-1180.
10. Pasternak O, Shenton ME, Westin CF. Estimation of extracellular volume from regularized multi-shell diffusion MRI In *15th International Conference on Medical Image Computing and Computer-Assisted Intervention (MICCAI)*, vol. 7512–2 of Lecture Notes in Computer Science. Nice, France, 2012:305-312.
11. Golub M, Henriques RN, Nunes RG. Free-water DTI estimates from single b-value data might seem plausible but must be interpreted with care. *Magn Reson Med*. 2021;85:2537-2551.
12. Hoy AR, Koay CG, Kecskemeti SR, Alexander AL. Optimization of a free water elimination two-compartment model for diffusion tensor imaging. *NeuroImage*. 2014;103:323-333.
13. Kaden E, Kruggel F, Alexander DC. Quantitative mapping of the per-axon diffusion coefficients in brain white matter. *Magn Reson Med*. 2016;75:1752-1763.
14. Descoteaux M, Angelino E, Fitzgibbons S, Deriche R. Regularized, fast, and robust analytical Q-Ball imaging. *Magn Reson Med*. 2007;58:497-510.
15. Hansen B, Jespersen SN. Data for evaluation of fast kurtosis strategies, b-value optimization and exploration of diffusion MRI contrast. *Sci Data*. 2016;3:160072
16. Westin CF, Maier SE, Mamata H, Nabavi A, Jolesz FA, Kikinis R. Processing and visualization for diffusion tensor MRI. *Med Image Anal*. 2001;6:93-108.

How to cite this article: Tristán-Vega A, París G, de Luis-García R, Aja-Fernández S. Accurate free-water estimation in white matter from fast diffusion MRI acquisitions using the spherical means technique. *Magn Reson Med*. 2021;00:1–8. https://doi.org/10.1002/mrm.28997